nature communications

Article https://doi.org/10.1038/s41467-025-64599-1

Ionomer engineering for optimized water channels in industry-scale water electrolysis using non-noble metal catalyst

Received: 6 February 2025

Accepted: 19 September 2025

Published online: 20 November 2025

Check for updates

Qisheng Yan[1,3], Cheng Liu[2,3], Weihang Li[1], Kai Sun[1], Yilin Zhou[1], Ning Han[1], Wenzhe Niu[1], Jinyan Chen[1], Xiao Yang[1], Junfeng Chen[1], Yixiang He[1], Zhuorong Lu[1], Youyong Li[2] & Bo Zhang[1]

The application of non-noble metal catalysts to replace high-cost iridium plays a critical role in the industrialization of proton exchange membrane water electrolysis (PEMWE). However, the activity and stability of non-noble metal catalysts are unsatisfactory especially at high current densities. This can partially be attributed to the limited water channels of Nafion ionomer in the catalyst layer which impede proton hydrate transport, resulting in a low local pH and accelerating non-noble metal dissolution. We propose that introducing an amphiphilic-like $CF_3CF_2CF_2CH_2OH$ molecule into Nafion ionomer (FOH-Nafion) via molecular engineering, optimizes the mass transfer of proton hydrates and therefore increase the stability of Co-based catalysts under high current densities. More dispersed and interleaved hydrophilic and hydrophobic regions of Nafion lead to efficient channels for proton hydrate transport. Such molecular engineering kept Co_3O_4 catalyst running over 270 h at 830 mA cm^{-2}, about 4 times that of the pristine Nafion ionomer. The molecular engineering strategy for the water channel in catalyst layer provides a pathway to improve the performance of non-noble metal catalysts in PEMWE.

Proton exchange membrane water electrolysis (PEMWE) powered by renewable solar or wind energy, is emerging as the most promising technology for industrial green hydrogen production[1–4]. Cobalt (Co)-based catalysts garner widespread attention for oxygen evolution reaction (OER) due to their catalytic activity and earth-abundant nature. However, instability under high current densities (>500 mA cm^{-2}) in PEMWE hinders their potential to replace costly iridium-based catalysts[1,2,5–10], limiting the industry-scale implementation of PEMWE. The metal dissolution at high current densities is mainly responsible for the instability of Co-based catalysts[11].

Concretely, in the membrane electrode assembly (MEA) system, the water channels are constructed by the sulfonate ion clusters of perfluorinated sulfonic acid (Nafion) ionomer film around the catalyst (Supplementary Fig. 1), which are critical for proton hydrate transport[12–14]. Nevertheless, these water channels are insufficient because most areas of Nafion are hydrophobic regions comprised of dense polytetrafluoroethylene (PTFE) backbone (Fig. 1b). Moreover, the water transport becomes specially tough at high current densities, because rapid water consumption and oxygen release will trigger gas-liquid cross-transmission congestion[15,16], considering limited water transport and low gas permeability of PTFE in Nafion ionomer film[17]. Under such harsh circumstance, the accumulated proton induced by inefficient water transport will decrease the local pH on the surface of catalysts, and the dissolution of Co ions from the oxide will be accelerated according to Pourbaix diagrams of Co-based materials[11,15]. Even worse, the dissolved Co ions can poison the sulfonate group and further hinder proton transport[15,18], which eventually forms the vicious circle. Therefore, it is imperative to optimize the water channels of

[1]State Key Laboratory of Molecular Engineering of Polymers, Department of Macromolecular Science, Fudan University, Shanghai, China. [2]Institute of Functional Nano & Soft Materials (FUNSOM) and Jiangsu Key Laboratory for Carbon-Based Functional Materials & Devices, Soochow University, Suzhou, China. [3]These authors contributed equally: Qisheng Yan, Cheng Liu. e-mail: bozhang@fudan.edu.cn

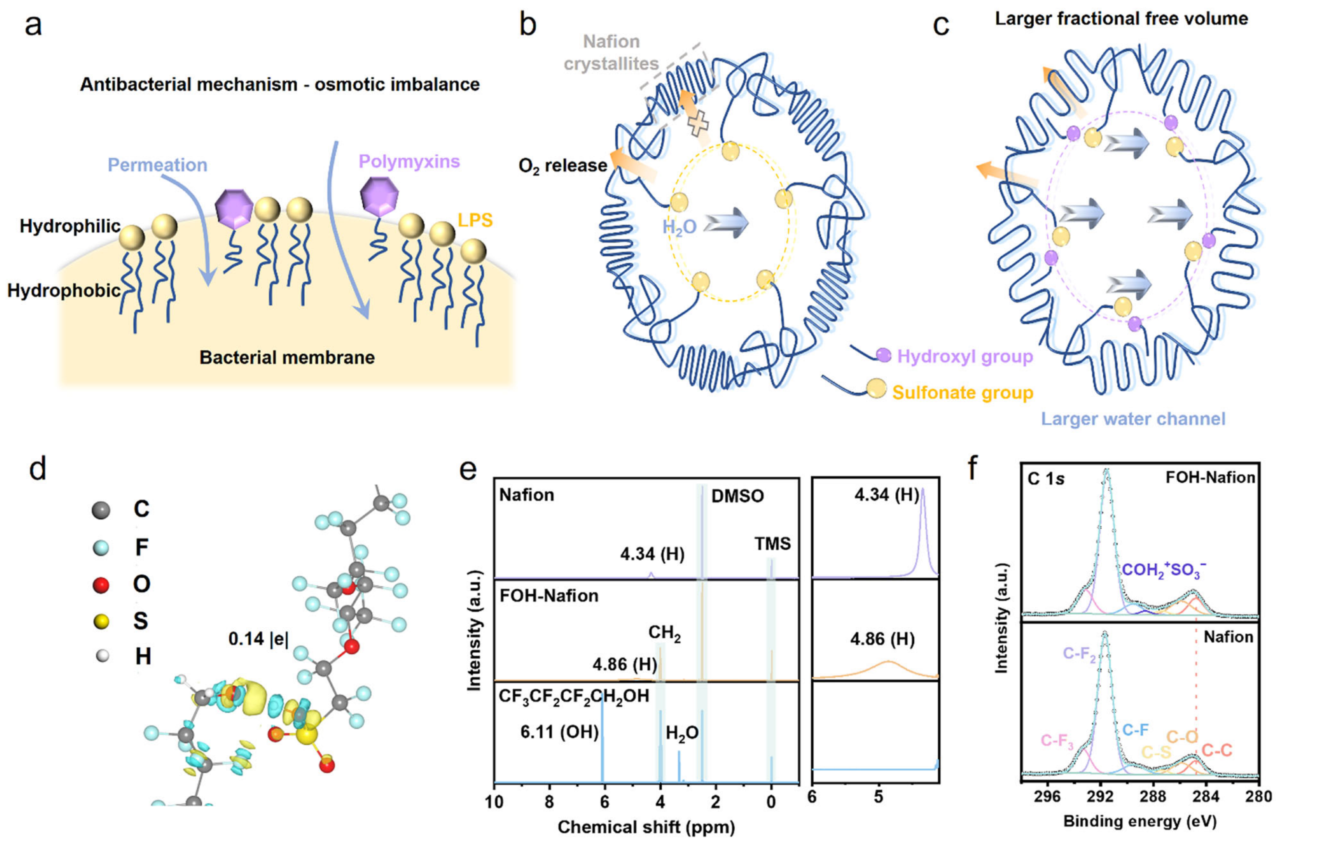

Fig. 1 | Structural analyses of FOH-Nafion ionomer. a Polymyxin consists of a cyclic heptapeptide head and a fatty acid tail which can interact with lipopolysaccharide (LPS) molecules of bacterial membrane to cause osmotic imbalance. **b** Traditional Nafion has a limited fractional free volume due to crystalline region. **c** The amphiphilic-like molecules interact with sulfonate groups and interfere with the ordered structure of PTFE, enlarging the fractional free volume and water channel. **d** Differential charge density distribution for the interaction between Nafion and $CF_3CF_2CF_2CH_2OH$ (isosurface value: ±0.003 e/Å^3). Yellow and blue regions represent electron accumulation and depletion, respectively. A pronounced charge transfer of 0.14 |e| from $CF_3CF_2CF_2CH_2OH$ to the sulfonate group of Nafion. **e** ^{1}H NMR spectra in DMSO-d_6 of Nafion, FOH-Nafion and $CF_3CF_2CF_2CH_2OH$. **f** C 1*s* XPS spectra of Nafion and FOH-Nafion. A new peak fitted at 288.6 eV is related to the formation of oxonium salt in FOH-Nafion. Source data are provided as a Source Data file.

Nafion ionomer in the catalyst layer to avoid the accumulation of proton.

Molecular modification of Nafion can contribute to high proton conductivity. He et al.[19] employed fluoroalkyl-grafted polyoxometalate (POMs) nanoclusters to modify Nafion membrane with great compatibility. The acidic POMs enhance proton conductivity by increasing proton content and hopping sites while their steric effects concurrently block hydrogen gas and vanadium ions permeation. However, for catalyst-layer ionomer, it does not need to be sealed like a membrane to impede the cross-transport of substances; instead, it requires unobstructed mass transfer channels. Appropriately disrupting the ordered structure of hydrophobic regions may be a strategy to facilitate water transport. In organisms, polymyxin, an effective antibiotic, inserts into bacterial membrane via electrostatic and hydrophobic interaction with lipopolysaccharide (LPS), disrupts the physical integrity of the membrane and then cause osmotic imbalance, leading to bacterial death (Fig. 1a)[20–22].

Inspired by the structure of polymyxin, we present a molecular engineering strategy, modifying Nafion ionomer with amphiphilic-like $CF_3CF_2CF_2CH_2OH$ molecules (FOH-Nafion). $CF_3CF_2CF_2CH_2OH$ is combined tightly with Nafion through coordination and hydrophobic interaction, resulting in the reduced crystallinity of PTFE phase and enlarged water channels. The proton migration is thus optimized to maintain the pH balance on the catalyst surface, thereby improving the stability of non-noble metals at high current densities. Besides, in situ electrochemical attenuated total reflection surface-enhanced infrared absorption spectroscopy (ATR-SEIRAS) disclosed unexpectedly that the oxonium salt structure protected active cobalt sites from being blocked by the sulfonate groups, ensuring sufficient active sites. As a result, FOH-Nafion/Co_3O_4 demonstrated a distinguished PEMWE performance, undergoing a 270-h constant current density of 830 mA cm^{-2} without obvious degradation.

Results

$CF_3CF_2CF_2CH_2OH$ can be considered as an amphiphilic-like molecule, with a hydroxyl group at one end and a fluoroalkyl at the other. As shown in Fig. 1c, hydroxyl groups of the doped molecules can interact with sulfonate groups to form oxonium salt ($COH_2^+SO_3^-$)[23]. To elucidate the interfacial interactions between $CF_3CF_2CF_2CH_2OH$ and Nafion, stable configurations of both species were optimized using density functional theory (DFT) calculations. Combined differential charge density and Bader charge analyses confirm a pronounced charge transfer of 0.14 |e| from $CF_3CF_2CF_2CH_2OH$ to the sulfonate group of Nafion (Fig. 1d and Supplementary data 1), implying strong electronic interaction. Moreover, free energy calculations reveal a substantial energy decrease as the sulfonate groups of Nafion and hydroxyl groups of $CF_3CF_2CF_2CH_2OH$ approach each other, suggesting their favorable interaction and its critical role in stabilizing the overall system (Supplementary Fig. 2). Beyond the electronic interaction, the hydrophobic fluoroalkyl tail can stably anchor in the PTFE domain of Nafion, which may disrupt the ordered folded chains of PTFE and enlarge the fractional free volume (FFV). Consequently, by

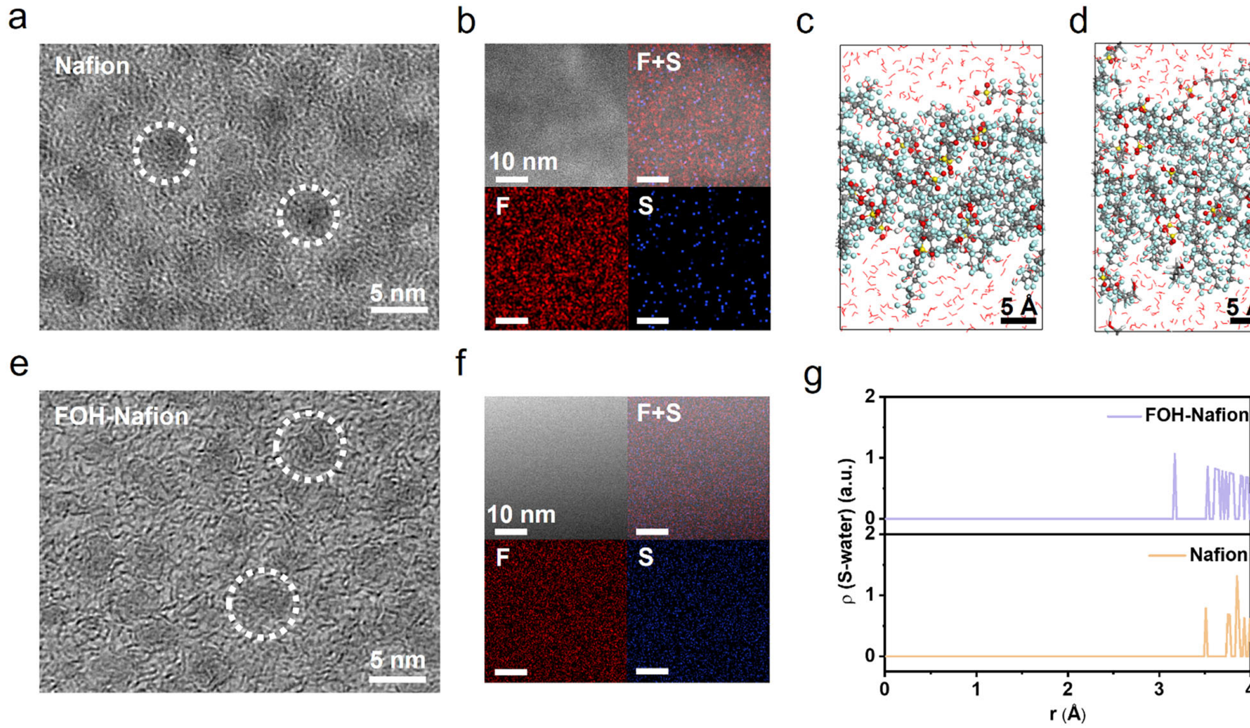

Fig. 2 | Morphology, composition distribution and molecular dynamics (MD) simulations of FOH-Nafion film. HR-TEM images of (**a**) Nafion and (**e**) FOH-Nafion. The marked dark regions represent the ionic cluster. The contrast of color in FOH-Nafion is much weaker than in Nafion. Spherical aberration-corrected HAADF-STEM images and XEDS elemental mappings of F (red) and S (blue) in (**b**) Nafion and (**f**) FOH-Nafion. F and S are more evenly dispersed in FOH-Nafion. Molecular models of (**c**) Nafion and (**d**) FOH-Nafion with water molecules (V-shape) after MD simulations. The Nafion molecule is represented by a ball-and-stick model, while $CF_3CF_2CF_2CH_2OH$ molecule is represented by a stick model (Supplementary Fig. 9). Element color codes: gray (C), cyan (F), red (O), white (H), yellow (S). **g** Radial density distribution profiles of S-H_2O in Nafion and FOH-Nafion, suggesting that FOH-Nafion is more accessible to the water molecule than Nafion. Source data are provided as a Source Data file.

mimicking natural systems, these structural modifications may facilitate water transport for pH balance and oxygen release under operating conditions.

To reveal the chemical structure of FOH-Nafion ionomer, we carried out ^{1}H nuclear magnetic resonance (NMR) spectrum measurement (Fig. 1e). The 4.34 ppm of chemical shift refers to the sulfonate group of commercial Nafion and 6.11 ppm is attributed to the hydroxyl group of $CF_3CF_2CF_2CH_2OH$. However, the two signals disappear in FOH-Nafion while a new signal appears at 4.86 ppm, demonstrating the coordination interaction between the sulfonate group and hydroxyl group, and the protons of the two groups have a similar chemical environment[23]. X-ray photoelectron spectroscopy (XPS) was conducted to investigate the formation of oxonium salt (Fig. 1f)[23,24]. Compared to Nafion, a new peak at 288.6 eV can be fitted from C 1*s* signal in FOH-Nafion, and is attributed to oxonium salt structure[23]. The binding energy of S 2*p* of FOH-Nafion becomes lower than that of Nafion (Supplementary Fig. 3), which can be attributed to the electron transfer from the hydroxyl group of $CF_3CF_2CF_2CH_2OH$ to the sulfonate group of Nafion. Differential scanning calorimetry (DSC) analysis (Supplementary Fig. 4) shows that three endothermic peaks observed at about 100, 205, and 218 °C represent evaporation of water, melting of the PTFE backbone crystalline phase, and rupture of ionic clusters, respectively[25]. FOH-Nafion shows a lower melting temperature (198 °C) than Nafion because of the reduced crystallinity. Moreover, the temperature of breakup of ionic clusters rises from 218 °C in Nafion to 229 °C in FOH-Nafion, indicating that the oxonium salt structure improves the stability of ionic clusters.

High-resolution transmission electron microscopy (HR-TEM) was used to reveal the morphology and structure of Nafion ionomer film (Fig. 2a and Supplementary Fig. 5). The circle marked dark areas (~4 nm in diameter) represent hydrophilic cluster regions composed of sulfonate groups in Nafion according to the previous research[19,26,27]. However, the hydrophilic regions in FOH-Nafion tend to extend into the hydrophobic regions with reduced color contrast (Fig. 2e). Further spherical aberration-corrected high-angle annular dark-field (HAADF) scanning TEM (STEM) images and corresponding X-ray energy-dispersive spectrometry (XEDS) elemental mapping show that the relaxed PTFE chains bring about more free volume, and the agglomerated sulfonate groups become more dispersed in PTFE (Fig. 2b, f). This suggests that the boundary between hydrophilic and hydrophobic phases tend to blur, and the hydrophilic phase gradually extends to the hydrophobic phase by the function of the amphiphilic-like molecule. X-ray diffraction (XRD) profiles for FOH-Nafion and Nafion membranes are shown in Supplementary Fig. 6. The diffraction peaks at 17.5°can be deconvoluted to two peaks at 16° and 17.5° which represent the amorphous and crystalline scattering from the main chain of Nafion, respectively[28,29]. The fitted integral area ratios show the declined crystallinity of FOH-Nafion compared to Nafion.

Small-angle X-ray scattering (SAXS) was conducted to deeply understand the microphase structural changes of Nafion caused by $CF_3CF_2CF_2CH_2OH$. We chose commercial Nafion 212 membranes as the qualitative research object. The SAXS profile of wet Nafion membrane shows two characteristic peaks (Supplementary Fig. 7). The first peak in the low-q region refers to the scattering of the long period among lamellar PTFE crystalline domains (including crystalline layers and amorphous layers) in the Nafion matrix[30,31]. The extracted parameters from correlation function curves qualitatively suggest that incorporating $CF_3CF_2CF_2CH_2OH$ into Nafion increases the long period, while decreases the crystallinity (Supplementary Table 1)[32], which is consistent with the XRD result. The second peak in the high-q region is

https://doi.org/10.1038/s41467-025-64599-1

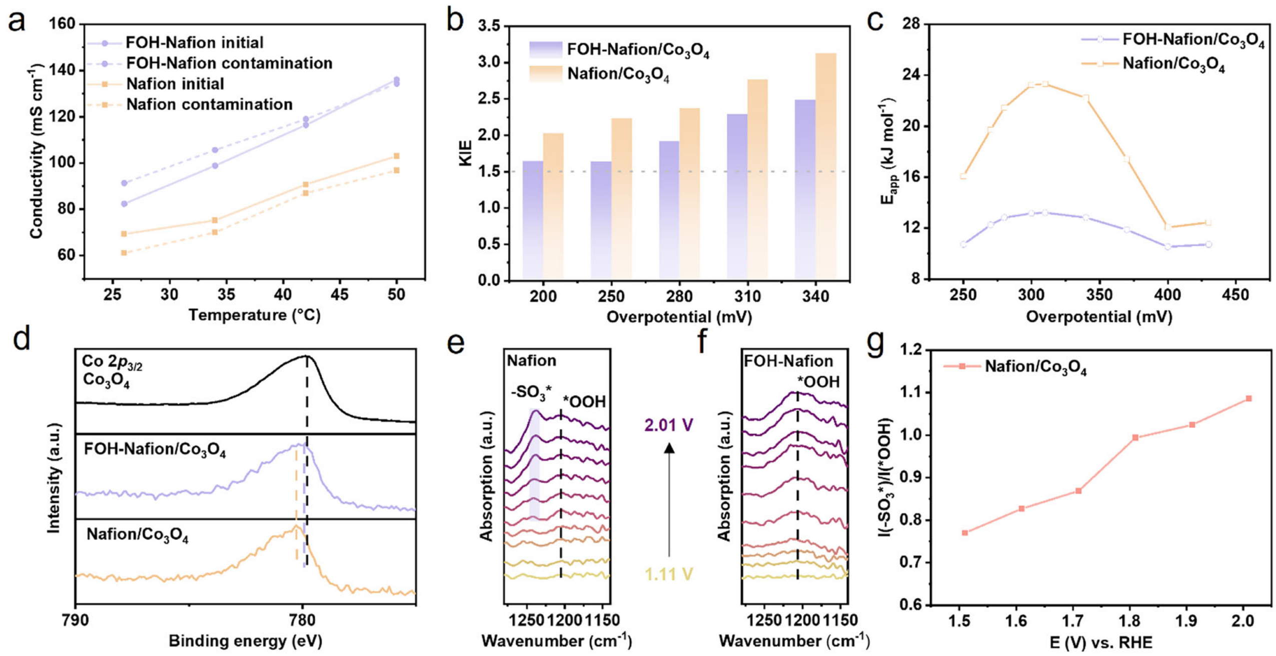

Fig. 3 | Electrochemical and spectroscopic characterizations of FOH-Nafion ionomer. a Proton conductivity of FOH-Nafion and Nafion membranes before and after Co^{2+} contamination calculated from EIS curves at 26, 34, 42, and 50 °C. **b** The KIE values against overpotential of Nafion/Co_3O_4 and FOH-Nafion/Co_3O_4 tested in a three-electrode system without a membrane in 0.5 M H_2SO_4. **c** The E_{app} plots against overpotential of Nafion/Co_3O_4 and FOH-Nafion/Co_3O_4. The corresponding E_{app} are calculated from CV curves recorded at different temperatures in 0.5 M H_2SO_4. **d** Co $2p_{3/2}$ XPS spectra of Co_3O_4, FOH-Nafion/Co_3O_4, and Nafion/Co_3O_4. In situ electrochemical ATR-SEIRAS spectra recorded in the potential range of 1.11 to 2.01 V with an interval of 0.1 V (vs. RHE) for (**e**) Nafion/Co_3O_4 and (**f**) FOH-Nafion/Co_3O_4 in 0.1 M $HClO_4$. **g** Intensity ratio of -SO_3* and *OOH measured at different potentials. Source data are provided as a Source Data file.

ascribed to the ionic cluster of sulfonate groups, also considered as the water channel[31]. The second peak of FOH-Nafion exhibits a low-q-shift (from 1.7 to 1.4 nm^{-1}), showing that FOH-Nafion has larger water channels (4.5 nm) than Nafion (3.7 nm)[13,33], contributing to H_2O and H_3O^+ transport. Water contact angle images exhibit that FOH-Nafion film has a better hydrophilic property than Nafion film (Supplementary Fig. 8). The calculated water uptake of FOH-Nafion membrane (19.1%) is also larger than that of Nafion membrane (14.2%), which is reasonable due to the enlarged water channels.

Molecular dynamics (MD) simulations concretely elucidated the optimization mechanism of mass transfer (Supplementary Fig. 9 and Supplementary data 1). The PTFE chains of Nafion interweave tightly with each other, detrimental to oxygen and water molecule passing through (Fig. 2c). Nevertheless, FOH-Nafion displays a loose chain arrangement that exposes more transfer pathways, and the sulfonate groups are more distributed (Fig. 2d), coinciding with the TEM images. To further quantify the interaction between sulfonate groups and water molecules, we also calculated the radial density distributions (RDS) and analyzed the intensity and distance of the first peak (Fig. 2g). The FOH-Nafion system exhibits a shorter S-H_2O distance compared to Nafion, accompanied by approximately 0.5-fold increase in the density profiles, indicating FOH-Nafion accommodates more water molecules within its bulk phase. Consequently, $CF_3CF_2CF_2CH_2OH$ could intervene in the ordered perfluorocarbon chains, render the hydrophilic and hydrophobic regions more intertwined and enlarge the water channels, which may not only promote oxygen release, but also facilitate water molecule transport.

We checked the effect of the oxonium salt on the apparent ionic exchange capacity (IEC) of the ionomers[34], and found that incorporating $CF_3CF_2CF_2CH_2OH$ into Nafion increases the IEC (Supplementary Table 2). Combined with the DFT calculation above, the interaction between the hydroxyl group of $CF_3CF_2CF_2CH_2OH$ and the sulfonate group activates the hydrogen of the hydroxyl group of $CF_3CF_2CF_2CH_2OH$, thus improving the exchange and migration capabilities of hydrogen ion[23]. Meanwhile, the reduced crystalline and enlarged water channels are also beneficial for exposing more sulfonate groups to access water, optimizing the proton transport network, thereby enhancing the apparent IEC. Proton conductivity measurements at different temperatures were also carried out to evaluate the transport of proton. As shown in Fig. 3a and Supplementary Fig. 10, the FOH-Nafion membrane exhibits higher proton conductivity than Nafion membrane. In addition, we also compared the proton conductivity after soaking the membrane in 0.2 mmol L^{-1} $Co(NO_3)_2$ solution to mimic Co ions dissolutive environment. It is noteworthy that the FOH-Nafion membrane remained its proton conductivity while Nafion membrane's proton conductivity reduced, suggesting that the oxonium salt structure enhances the resistance of the sulfonate group to ion's contamination, which is significant to the proton migration.

In order to explore the effect of proton transfer on the OER process, we performed a series of electrochemical experiments in a standard three-electrode system. We synthesized the Co_3O_4 according to the previous research with some modifications[35] (Supplementary Fig. 11). The gas diffusion electrode (GDE) with the same Co_3O_4 catalyst on carbon paper was used during the test. Firstly, cyclic voltammetry (CV) curves were obtained to study the effect of FOH-Nafion ionomer on the redox properties of Co_3O_4. No obvious differences were observed in the CV curves of FOH-Nafion/Co_3O_4 and Nafion/Co_3O_4 (Supplementary Fig. 12). Therefore, FOH-Nafion ionomer cannot affect the redox properties of the catalyst itself.

Kinetic isotope effect (KIE) is a classic experimental technique to investigate chemical reactions closely related to proton transfer[36,37]. We collected the linear sweeping voltammetry (LSV) curves of both FOH-Nafion/Co_3O_4 and Nafion/Co_3O_4 GDEs in the protonic (0.5 M H_2SO_4 in H_2O) vs. deuteric (0.5 M D_2SO_4 in D_2O) solution to investigate the KIE of acidic OER (Fig. 3b and Supplementary Fig. 13). The KIE values were estimated based on the ratio of the current densities in the protonic and deuteric solution at the same overpotential[38]. When the KIE decreases below 1.5, it reflects a transition from primary KIE to secondary KIE, indicating that the rate-limiting step shifts from involving proton transfer to not involving proton transfer[36,38,39]. The observed increase in KIE with rising overpotential probably originate from the intrinsic OER of catalyst, like accelerated electron transfer, surface reconstruction[38,40,41], or enhanced steric hindrance caused by increased surface intermediate coverage[40,42]. Such effects distinctly manifest the proton-transfer limitation, making it the dominant kinetic bottleneck in the OER process. Although both systems exhibit KIEs >1.5, FOH-Nafion/Co_3O_4 shows smaller KIE than Nafion/Co_3O_4 at the same overpotential, indicating improved proton-transfer kinetics during the OER process. Given that the identical catalyst was used during the measurements without Nafion membrane, this difference could be attributed to the ionomer effect on the local microenvironment[43]. Additionally, FOH-Nafion membrane maintained higher deuteron conductivity compared to Nafion membrane (Supplementary Fig. 14), and further prove that the optimized water channels of FOH-Nafion enhance the deuteron transfer. Overall, the enhanced proton conductivity and apparent IEC of FOH-Nafion ionomer facilitate proton transfer, thereby accelerating the OER process.

Temperature-dependent kinetic analysis was conducted to draw the curve of apparent activation energy (E_{app}) against overpotential. The LSV curves were recorded in 0.5 M H_2SO_4 solution in the temperature range of 20–60 °C (Supplementary Fig. 15). The performance of FOH-Nafion/Co_3O_4 and Nafion/Co_3O_4 GDEs enhanced with elevated temperature, inferring that the OER process was controlled by thermodynamics. Note that the E_{app} values of both reached their maximum at the same overpotential of about 310 mV (Fig. 3c), which is usually consistent with catalytic OER onset potential[38]. This indicates that the modification of the ionomer did not change catalyst's intrinsic activity which affects the onset potential[38]. Interestingly, the maximum of E_{app} value of FOH-Nafion/Co_3O_4 was 13.2 kJ mol^{-1}, nearly half of that of Nafion/Co_3O_4. The reduced E_{app} could be attributed to the favorable water replenishment and proton transfer on the active sites of Co_3O_4 catalyst.

The X-ray photoelectron spectroscopy (XPS) was obtained to gain insight into the impact of Nafion ionomer on the surface structure of Co_3O_4. The binding energy of Co $2p_{3/2}$ shifted to higher direction in Nafion/Co_3O_4 compared to blank Co_3O_4 (Fig. 3d and Supplementary Fig. 16). It is reported that a similar shift in the Pt $4f_{7/2}$ peak was observed due to adsorption of sulfonate groups on Pt/C[23]. This suggests that sulfonate groups may also adsorb on the Co_3O_4 surface. However, the peak in FOH-Nafion/Co_3O_4 was closer to that in blank Co_3O_4, implying that the formed oxonium salt structure prevent Co sites from being adsorbed by sulfonate groups[23].

Furthermore, we exploited in situ electrochemical ATR-SEIRAS to monitor intermediate variation of Co_3O_4 at a continuously varying potential vs. RHE in 0.1 M $HClO_4$ (Fig. 3e, f). The configuration of custom-built electrochemical cells is shown in Supplementary Fig. 17. It is noteworthy that both Nafion/Co_3O_4 and FOH-Nafion/Co_3O_4 samples exhibited an evident peak at 1204 cm^{-1} and 1207 cm^{-1}, respectively, upon reaching 1.51 V (280 mV overpotential). The overpotential of peak's emergence is close to the OER onset potential and the peak showed no appreciable potential-dependent shift but displayed increasing intensity with enhancing applied potential, suggesting it represents the active intermediate species (*OH, *O, *OOH and *OO in Supplementary Fig. 18). Both *OH and *O species can be excluded as their peaks fall outside the 1220–1000 cm^{-1} range[44–47], whereas the stretching vibration peaks of *OOH and *OO species are consistently reported within this spectral region[47–52]. Isotopic labeling experiments were conducted in 0.1 M $HClO_4/D_2O$ electrolyte, the original 1204 cm^{-1} peak in Nafion/Co_3O_4 disappeared, replaced by a new feature at 1179 cm^{-1}, showing a redshift[47,50], which also happened in FOH-Nafion/Co_3O_4 (Supplementary Fig. 18). Therefore, this peak could be attributed to the stretching vibration of *OOH based on the previous research[49,51]. A peak at about 1238 cm^{-1} was observed at 1.51 V in Nafion/Co_3O_4 and the intensity became stronger with increasing potential, which was caused by the adsorption of sulfonate group[53,54]. To unveil the competitive adsorption of *OOH species and sulfonate group to cobalt site, we plotted the intensity ratio of -SO_3* and *OOH in Nafion/Co_3O_4 against potential vs. RHE. As shown in Fig. 3g, the ratio rose with increasing potential, indicating that the active cobalt site tended to be blocked by the sulfonate group especially at high potentials, leading to the gradual degradation of the activity in the traditional ionomer system. However, no adsorption peak of sulfonate group was observed in FOH-Nafion/Co_3O_4 with increasing potential, indicating that the oxonium salt structure remained stable and continuously protected the active sites from being blocked by the sulfonate group, which is beneficial for the overall stability of PEMWE. The electrochemical active surface area (ECSA) measurements also illuminate that the modified Nafion enables increased exposure of Co active sites (Supplementary Fig. 19). The DFT calculations could also suggest that the distance between S and Co increased due to the steric hindrance of the formed oxonium salt structure, reducing the possibility of sulfonate groups adsorption on Co sites (Supplementary Fig. 20 and Supplementary data 1).

Scanning electron microscopy (SEM) was used to observe the catalyst layer of FOH-Nafion/Co_3O_4 MEA. FOH-Nafion ionomer does not change the surface morphology of the catalyst layer in MEA (Supplementary Fig. 21). Further cryogenic focused ion beam/SEM (cryo-FIB/SEM) was employed to reveal a more detailed ionomer-catalyst distribution (Fig. 4a–c; Supplementary Fig. 22). As shown in Fig. 4b, c, the ionomer uniformly envelops the catalyst particles like a spiderweb. Notably, the modified Nafion does not significantly alter the pore structure of the ionomer-catalyst distribution. Thus, the performance variation is mainly attributed to the optimized mass transport channels resulting from microstructural phase changes in the Nafion ionomer.

The practicality of FOH-Nafion ionomer was confirmed in PEMWE. Figure 4d, e shows current-voltage polarization curves in the PEMWE. The FOH-Nafion/Co_3O_4 MEA requires a voltage of 1.70 V reaching the current density of 490 mA cm^{-2}, similar to Nafion/Co_3O_4 MEA. Cyclic square-wave voltammetry can examine the operational stability under dynamic condition to mimic the coupling of water electrolysis and wind/solar-power[2]. After 5000 cycles swinging between 1.40 V to 1.75 V with 10-s residence time at every voltage, FOH-Nafion/Co_3O_4 MEA shows better repeatability. Notably, FOH-Nafion/Co_3O_4 and Nafion/Co_3O_4 MEAs exhibit minimal differences in post-cycling current density at lower voltages (e.g., 1.60 V), but the current density of Nafion/Co_3O_4 MEA declines to 360 mA cm^{-2} at 1.70 V. As discussed above, this observation certainly demonstrates that optimizing the water channels within Nafion ionomer can effectively enhance the stability of Co_3O_4 catalyst under higher current densities or elevated voltages. Faradaic efficiencies (FEs) for the anode in PEMWE were measured at the current densities of 167, 500, and 1000 mA cm^{-2} (Supplementary Fig. 23). An average FE of 98.7% was obtained, indicating that the FOH-Nafion ionomer do not cause other electrochemical reaction.

To investigate the water transport resistance, electrochemical impedance spectroscopy (EIS) measurements were carried out based on the MEA system (Fig. 4f and Supplementary Table 3). When a voltage of 1.75 V was applied, the mass-transfer resistance became apparent at low frequency due to large water consumption and oxygen production. The fitting results indicate that FOH-Nafion dramatically decreases both charge-transfer (R_{ct}) and mass-transfer (R_{mt}) resistance. This is consistent with speculation, namely, the optimized water channels and loose carbon-fluorine chain regions promote water access to active Co sites and proton migration.

Finally, we performed chronopotentiometry tests at the constant current density of 830 mA cm^{-2} to evaluate the stability of FOH-Nafion/Co_3O_4 MEA in PEMWE. We firstly evaluated the stability of modified Nafion with different $CF_3CF_2CF_2CH_2OH$ doping ratios (Fig. 4g and Supplementary Fig. 24). All modified Nafion samples demonstrates enhanced performance compared to pristine Nafion and the 1:1 doping

 https://doi.org/10.1038/s41467-025-64599-1

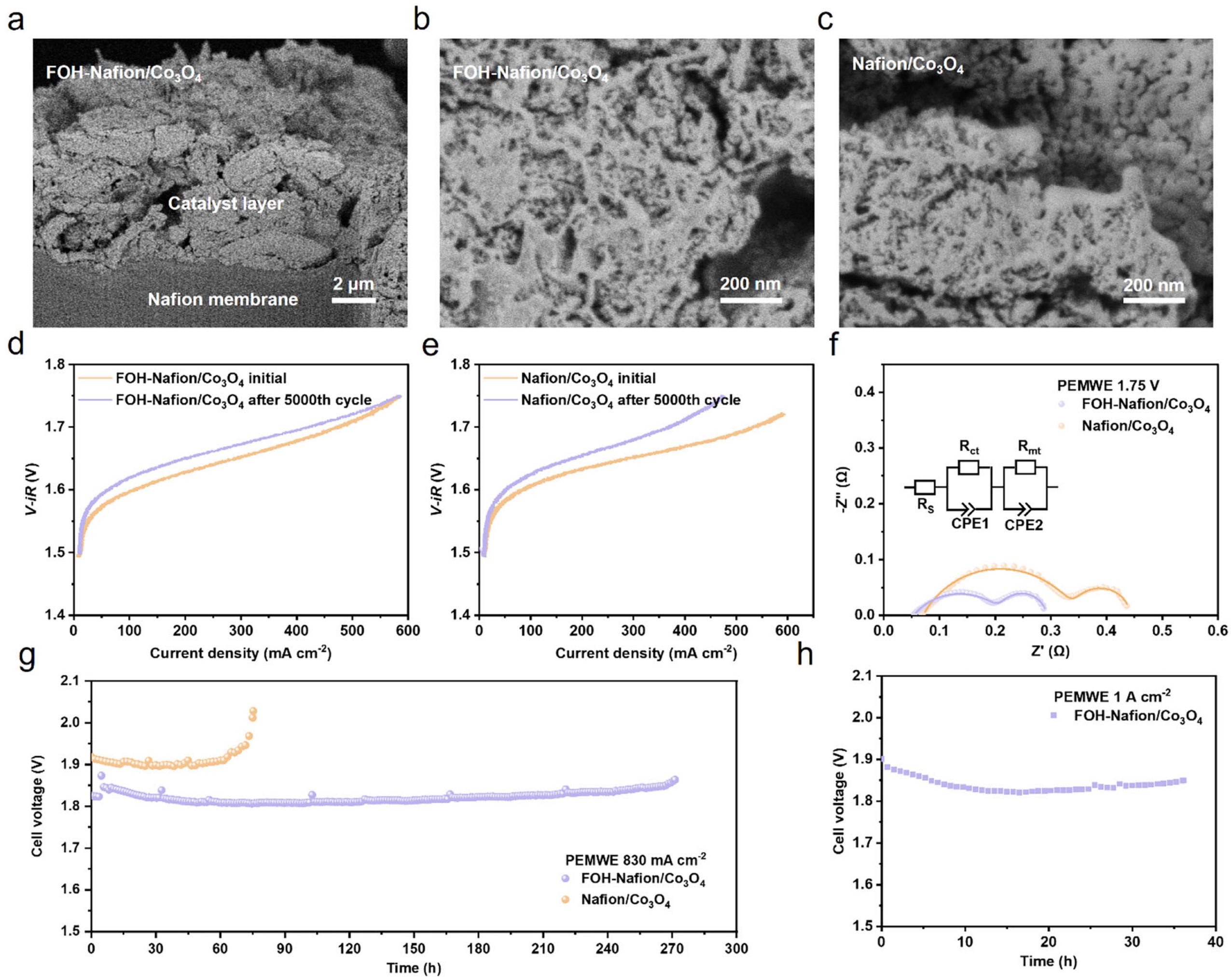

Fig. 4 | Structure and PEMWE performance of MEAs. Cryo-FIB/SEM images of (**a**, **b**) FOH-Nafion/Co_3O_4 and **c** Nafion/Co_3O_4 MEAs. Current-voltage polarizations of the PEMWE after 5000 multiple-voltage cycles of (**d**) FOH-Nafion/Co_3O_4 and (**e**) Nafion/Co_3O_4 with iR correction. The stepwise voltage swings between 1.4 V and 1.75 V with 10 s dwell time at each voltage. **f** EIS curves of PEMWE and fitting curves at 1.75 V, inset showing equivalent circuit. **g** Chronopotentiometry test of FOH-Nafion/Co_3O_4 and Nafion/Co_3O_4 at 830 mA cm^{-2}. **h** Chronopotentiometry test of FOH-Nafion/Co_3O_4 at 1 A cm^{-2}. The input water was controlled at 80 °C. Source data are provided as a Source Data file.

ratio exhibited optimal balance between cell voltage and operational stability. The FOH-Nafion/Co_3O_4 MEA shows good operational stability, remaining around 1.81 V for 270 h without obvious degradation. In contrast, the conventional Nafion/Co_3O_4 MEA exhibited a sharp potential increase from 1.90 V after only 70 h of operation. This pronounced contrast unequivocally confirms the durable effectiveness of the FOH-Nafion ionomer. Moreover, FOH-Nafion/Co_3O_4 MEA sustained a voltage of 1.84 V under a high current density of 1 A cm^{-2} for 35 h (Fig. 4h), showing the prospect of industrial application. Since $CF_3CF_2CF_2CH_2OH$ molecule is insoluble in water and its fluoroalkyl end has better compatibility with the PTFE matrix of Nafion, the small molecule is not easy to leach out (Supplementary Fig. 25). To gain insights into the structural evolution of FOH-Nafion during OER process, post-reaction XPS characterization subjected to 0.1 M $HClO_4$ electrolyte was conducted (Supplementary Fig. 25). The C 1s spectrum still shows the characteristic peak of oxonium salt, confirming the considerable stability of FOH-Nafion under OER conditions. Compared to previously reported non-noble metal catalysts in PEMWE (Supplementary Table 4), FOH-Nafion/Co_3O_4 exhibits a competitive performance, suggesting that regulating the ionomer structure to optimize the water channel is effective and is a potential strategy to achieve the industrial application of non-noble metal catalysts in the future.

Inductively coupled plasma-mass spectrometry (ICP-MS) was used to investigate the dissolution of cobalt. Time-dependent dissolution profiles suggest that FOH-Nafion ionomer effectively suppressed cobalt leaching (Supplementary Fig. 26), evidencing the stabilization effect of FOH-Nafion ionomer on the Co_3O_4 catalyst. The Co_3O_4 derived from ZIF-67 (ZIF-Co_3O_4) was also synthesized referring to the reported method[55]. Noted that ZIF-Co_3O_4 still showed considerable stability used with FOH-Nafion ionomer compared to Nafion ionomer at 500 mA cm^{-2} in PEMWE (Supplementary Fig. 27), proving the applicability of this modified ionomer to Co_3O_4 catalysts.

Discussion

In summary, we introduced $CF_3CF_2CF_2CH_2OH$ into Nafion ionomer to simulate the polymyxin invasive mechanism of bacterial membranes to optimize water channels and promote the proton hydrate transport. Meanwhile, the adsorption of sulfonate groups to cobalt sites can be prevented to expose more active sites. Through the molecular engineering strategy, FOH-Nafion/Co_3O_4 MEA achieves a fourfold improvement in stability at 830 mA cm^{-2} and even operates stably for 35 h under an industrial-grade current density of 1 A cm^{-2}, showing the potential of non-noble metal catalyst for application in PEMWE. This inspires us not only to focus on the intrinsic activity and stability of the catalyst, but also to consider the influence of the ionomer in actual engineering devices.

Methods

Chemicals

2,2,3,3,4,4,4-Heptafluoro-1-Butanol ($CF_3CF_2CF_2CH_2OH$, ≥98%) was purchased from Adamas. 5% Nafion® ionomer solution and Nafion 212 membrane were obtained from DuPont. $CoCl_2{\cdot}6H_2O$ (≥99%), H_2SO_4 (95.0–98.0%), NaOH (≥96.0%), 2-methylimidazole (98%), ethanol (≥99.7%) and methanol (≥99.5%) were obtained from the Sinopharm Chemical Reagent Co., Ltd. 1H-Benzotriazole (1H-BTA) (99%), $Co(NO_3)_2{\cdot}6H_2O$ (≥99%) and $HClO_4$ (70.0–72.0%) were purchased from Aladdin. As for carbon paper (CP), TGP-H-060 was provided by Toray and Sigracet 28BC was from the Fuel Cell Store. 40% Pt/C catalyst was obtained from Johnson Matthey Company. Platinum plated titanium felt was purchased from NV Bekaert SA. Pure water was used in all processes. All chemicals were used without purification.

Synthesis of $CF_3CF_2CF_2CH_2OH$ modified Nafion (FOH-Nafion)

$CF_3CF_2CF_2CH_2OH$ was added into 5% Nafion ionomer solution with controlled 1:1 weight ratio of $CF_3CF_2CF_2CH_2OH$ and Nafion. Then the mixture was stirred at 60 °C for 6 h in a sealed container. The obtained solution was ready for use. Unless otherwise specified, the doping ratio is defaulted to 1:1. Samples with other doping ratios (0.5:1, 2:1) were synthesized by the same way.

Synthesis of Co_3O_4 powder catalyst

The Co_3O_4 catalyst was synthesized according to the previous research with some modifications[35]. To be specific, 0.70 g of $CoCl_2{\cdot}6H_2O$ was dissolved in 50 mL of water to form A solution. 0.60 g of NaOH and 0.60 g of 1H-BTA were dissolved in 100 mL of water to obtain B solution. Then the A solution was quickly added into the B solution and kept stirring at room temperature for 12 h. After that, the mixture was filtered and washed with water three times. Finally, the obtained sediments were dried at 60 °C overnight under vacuum. The as-synthesized sample was then calcinated at 350 °C for 6 h to transform to Co_3O_4. ZIF-Co_3O_4 was synthesized based on the previous research with some modifications[55]. Briefly, 0.87 g of $Co(NO_3)_2{\cdot}6H_2O$ was added into 30 mL of methanol. 1.97 g of 2-methylimidazole was added into 30 mL of methanol. Then the two solutions were mixed under vigorous stirring and then the mixture was incubated at room temperature for 24 h. The precipitates were centrifuged, and washed with methanol three times. Finally, the obtained sediments were dried at 60 °C overnight. The purple powder was then annealed at 350 °C for 2 h and the obtained sample was denoted as ZIF-Co_3O_4.

Fabrication of gas diffusion electrode (GDE)

The GDE composed of Co_3O_4, ionomer, and TGP-H-060 carbon paper (or platinum plated titanium felt). The ink of Co_3O_4 catalyst was prepared by ultrasonically blending the catalyst with Nafion solution and ethanol. The Nafion ionomer-to-catalyst ratio was controlled in 0.3, and the catalyst loading was controlled in 2 mg cm^{-2}. Then the ink was sprayed on the carbon paper at the hot plate. The tested area was controlled within 0.25 cm^2.

Nafion membrane pretreatment

A commercially available Nafion 212 membrane (thickness, 58 µm) was used for synchrotron radiation SAXS, XRD tests and conductivity experiments. The FOH-Nafion 212 membrane was prepared by immersing the Nafion 212 membrane in a certain amount of $CF_3CF_2CF_2CH_2OH$. For SAXS experiments and conductivity experiment, to monitor the microstructure of the membranes in the wet state, both the FOH-Nafion membrane and the pristine Nafion membrane were soaked in the pure water overnight before the tests. For other characterizations, the FOH-Nafion and Nafion films were obtained from the ionomer solution by the casting method. For PEMWE test, the Nafion 212 membrane was used directly.

Characterizations

The ^1H NMR spectra of different materials were detected by A Bruker VANCE NEO at 600 MHz. Samples were dissolved in dimethyl sulfoxide (DMSO)-d_6 with tetramethyl silane (TMS) as internal standard. The X-ray diffraction (XRD) patterns of membrane were performed with a point step of 0.02 degree by a Rigaku Smatlab 9KW with a HyPix-3000 detector using Cu Kα radiation. The surface morphology of catalysts was acquired by Scanning electron microscopy (SEM) using Bruker operated at 1.0 kV. The high-resolution transmission electron microscopy (HR-TEM) images were measured by a JEOL JEM-2100F transmission electron microscope. Spherical aberration-corrected High-angle annular dark-field (HAADF) scanning TEM (STEM) images and corresponding X-ray energy-dispersive spectrometry (XEDS) elemental mapping were obtained by Thermofisher Spectra 300 with a SuperX detector. The X-ray photoelectron spectroscopy (XPS) was conducted using a Thermo Scientific K-Alpha+ equipped with an Al Kα X-ray source (1486.6 eV) for excitation. All peak energies were calibrated against the binding energy of C 1*s* peak, which was fixed at 284.8 eV. The XPS data was analyzed using the Thermo Avantage Software. Differential scanning calorimetry (DSC) experiments were performed with a DSC 250 instrument (TA instruments, USA). About 10 mg of solid samples were used for the analysis. The analyses were carried out at a heating rate of 10 °C min^{-1} up to a temperature of 280 °C. Water contact angle of Nafion films tests were performed using Biolin Scientific Attension® Theta.

Small angle X-ray scattering (SAXS) study

SAXS measurements were performed by Xeuss 2.0 (Xenocs, France) with a radiation source of Cu Kα X-ray (λ = 0.154 nm). The scattering two-dimensional (2D) patterns were collected by a surface detector of Pilatus3R 200K-A (490 × 400 pixels). The sample to detector distance was 123 cm. All data were corrected for background (dark current) and the sensitivity of each pixel in the area detector. One-dimensional (1D) curves were obtained by integrating 2D patterns from 0 to 360° using Foxtrot software. The scattered wavevector $\boldsymbol{q}$ is given by the Eq. (1):

$$q = \frac{4\pi sin\theta}{\lambda} \tag{1}$$

where λ is the beamline wavelength and θ is the scattering angle. The correlation function corresponds to the Fourier transform of the intensity function and the 1D correlation function is given by the expression (2)[32]:

$$\gamma(r) = \frac{1}{Q}\int_0^\infty I(q)q^2cos(qr)dq \tag{2}$$

where Q means extrapolated invariant used to normalize the transform so that $\gamma(0) = 1$. r refers to distance. The SasView software was applied to the analyze SAXS data.

Ion exchange capacity (IEC) measurements

The apparent IEC (titrimetry value) of ionomers was measured by titrimetry[34]. The dry ionomers were immersed in 50 mL of NaCl (2.0 M) solution for 2 h and titrated with NaOH (0.01 M) by automatic potentiometric titrator. The IEC (meq g^{-1}) was calculated using the expression (3):

$$IEC = \frac{V(NaOH) \times C(NaOH)}{m(ionomer)} \tag{3}$$

where m(ionomer) means the mass of dry ionomer, V(NaOH) means the consumption volume of NaOH solution, and C(NaOH) means the concentration of NaOH solution.

In situ electrochemical attenuated total reflection surface-enhanced infrared absorption spectroscopy (ATR-SEIRAS) measurements.

In situ electrochemical ATR-SEIRAS measurements were performed in Bruker INVENIO infrared spectrophotometer. The spectral resolution of FTIR spectra is 4 cm^{-1} and the acquisition time of each spectrum is about 14 s. The working electrode consisted of an Au thin film deposited on a Si prism by two steps[56,57]. Firstly, the Si prism's reflecting plane was first mechanically polished using 0.3 and 0.05 μm Al_2O_3 powders, and soaked in piranha solution to make the surface oxidized. Subsequently, the reflecting plane was etched in a 40% NH_4F solution for 1.5 min. A gold film was then deposited by immersing the reflecting plane in a plating solution at 60 °C for 3 min. The plating solution is composed of 0.015 M $HAuCl_4$, 0.05 M $Na_2S_2O_3$, 0.15 M Na_2SO_3, and 0.05 M NH_4Cl. Finally, the catalyst ink was dropped on the Au film and dried at room temperature. The electrolyte was 0.1 M $HClO_4$ (pH = 1.00 ± 0.03) and freshly prepared before each measurement. A graphite rod and a Hg/Hg_2SO_4 were used as the counter electrode and reference electrode, respectively. The electrode potential was maintained at the open circuit potential (OCP) while a background spectrum was collected. All spectra are displayed in absorbance units, defined as -log(I/I_0), where I and I_0 refer to the reflected radiation intensity of the sample and the background spectrum, respectively. The electrode potential scanned from 0.2 to 1.3 V vs. Hg/Hg_2SO_4. The potential is presented without iR correction.

Electrochemical measurements

Electrochemical studied were performed using a three-electrode system by an electrochemical workstation (Autolab PGSTAT204) equipped with a built-in electrochemical impedance spectroscopy (EIS) analyzer. The GDE is exploited as a working electrode. Pt foil and Hg/Hg_2SO_4 were used as the counter and reference electrodes, respectively. 0.5 M H_2SO_4 (pH = 0.30 ± 0.05) was used as the electrolyte and freshly prepared before each measurement. Cyclic voltammetry (CV) test at 50 mV s^{-1} was conducted for 5 cycles before collecting linear scan voltammetry (LSV) at 5 mV s^{-1} for each sample. The electrode potentials were calibrated to the RHE scale by the Eq. (4):

$$E(RHE) = E(Hg/Hg_2SO_4) + 0.652V + 0.059pH \tag{4}$$

The applied potential with iR compensation is denoted as *V-iR* specially.

Kinetic isotope effect (KIE) investigation. The electrochemical measurements of the FOH-Nafion/Co_3O_4 were performed in protonic (0.5 M H_2SO_4 in H_2O) and deuteric (0.5 M D_2SO_4 in D_2O) electrolytes, respectively. The pD of the deuteric solution was calculated by adding 0.41 to the measured pH value[38]. The potentials on RDE scale were calculated using equation:

$$E(RDE) = E(Hg/Hg_2SO_4) + 0.652V + 0.059\text{pD} + 0.013V \tag{5}$$

The OER overpotentials η in the protonic and deuteric electrolytes were calculated by Eqs. (6) and (7), respectively:

$$\eta = E(RHE) - 1.23V \tag{6}$$

$$\eta = E(RDE) - 1.26V \tag{7}$$

The KIE value was finally calculated by the Eq. (8):

$$KIE = \left|\frac{j_H}{j_D}\right|_\eta \tag{8}$$

where j_H and j_D refer to the current density at the same overpotential in the protonic and deuteric electrolytes, respectively.

Apparent activation energy acquisition. The LSV curves of GDE were collected to extract the apparent activation energy (E_{app}) for the acidic OER at different temperatures (20, 30, 40, 50, and 60 °C). For heterogeneous electrocatalytic reaction, E_{app} can be deduced from fitting the slope of the Arrhenius plot using the Eq. (9):

$$\left|\frac{\partial(\log_{10} j)}{\partial(1/T)}\right|_\eta = -\frac{E_{app}}{2.303R} \tag{9}$$

where j is the current density, R is the ideal molar gas constant (8.314 J mol^{-1} K^{-1}) and T is the temperature (K).

Water uptake (*WU*). The dried membrane was measured as dry weight (W_{dry}) and then fully hydrated in water for 8 h at room temperature. After removing surface water, the weight (W_{wet}) of wet membrane was re-measured. The value of water uptake was computed using the Eq. (10):

$$WU = \frac{(W_{wet} - W_{dry})}{W_{dry}} \times 100\% \tag{10}$$

Proton conductivity measurements of membranes. EIS measurements were performed to explore the in-plane proton conductivity of the membranes using the two-electrode cell at different temperatures (26, 34, 42, and 50 °C) with a frequency scan range from 1000 kHz to 1 Hz with an amplitude of 5 mV. The prepared membranes were assembled into the cell and immersed in pure water (or D_2O). The in-plane proton conductivity σ of the membrane was calculated by the equation[28] (11):

$$\sigma = \frac{l}{R_m \times t \times w} \tag{11}$$

where the resistance data R_m was acquired from the EIS spectra, the distance l between the two electrodes is 1 cm, and w and t denote the width (1 cm) and thickness of the membrane, respectively. To examine the anti-poisoning ability of Nafion, we immersed the tested membranes into 0.2 mmol L^{-1} $Co(NO_3)_2$ solution for 3 h and then tested the proton conductivity again.

Electrochemical active surface area (ECSA) of each catalyst was derived from the electrochemical double-layer capacitances (C_{dl}) by recording the scan rate CV-dependence plot in a non-Faradaic region. The CV cycle potential window was 0.3 to 0.4 V vs. Hg/Hg_2SO_4, and the scan rates were 6, 8, 10, and 12 mV s^{-1}. The difference of current density (Δj) between charging and discharging process at the average potential in the selected range was calculated from Eq. (12):

$$\Delta j = \frac{1}{2}(j_{charge} - j_{offcharge}) \tag{12}$$

The slope of the linear fit was calculated as the C_{dl}. A specific capacitance of 40 μF cm^{-2} was used here[53]. The ECSA of the catalyst was calculated from the following Eq. (13):

$$ECSA = \frac{C_{dl}}{40\mu F cm^{-2}} cm^2{}_{ECSA} \tag{13}$$

A proton exchange membrane water electrolysis (PEMWE) test was carried out on the DC power source (PWR401L, KIKUSUI Trading Co., Ltd.). Membrane electrode assembly (MEA) was fabricated by the spraying method. The ink of Pt/C catalyst was prepared by ultrasonically blending catalyst with Nafion solution and ethanol. The Nafion® ionomer-to-catalyst ratio was 0.3. The cathodic side was prepared at 80 °C by spraying Pt/C ink onto the Nafion membrane, and the loading was controlled at 0.3 $mg_{Pt}\ cm^{-2}$. The anodic side was prepared by the same way and catalyst's loading was controlled at 2 mg cm^{-2}. Then the catalyst-coated membrane was hot pressed at 1 MPa for 5 min at 80 °C. Platinum plated titanium felt and carbon paper (Sigracet 28BC) were taken as the current collector on the anodic and cathodic sides, respectively. They were closely assembled against the titanium plates with a torque of 1 N·m in the single cell. Both sides of the cell contain serpentine flow channels, and the active area was 3 cm^{-2}. The 80 °C pure water was fed to the anodic side of the cell at a flow rate of 120 mL·min^{-1}. EIS data were recorded with a frequency scan range from 100 kHz to 0.01 Hz with an amplitude of 10 mV at 1.75 V. Cyclic square-wave voltammetry was conducted between 1.40 V to 1.75 V with 10-s residence time at every voltage.

Inductively coupled plasma-mass spectrometry (ICP-MS) measurements (by Agilent 7700). The measured liquid at the anodic outlet of PEMWE was collected at 24 h intervals throughout the 72-h durability test.

Faradaic efficiency (*FE*) of O_2 produced in PEMWE was measured by drainage method. After the voltage was stable delivering the current density of 167, 500 and 1000 mA cm^{-2}, the generated anodic gas flowed into the bottle containing water, and the volume of the discharged water was measured to obtain the gas volume. *FE* was calculated from the Eq. (14):

$$FE = \frac{4F \times n_{O2}}{Q} \times 100\% \tag{14}$$

where *F* is the Faraday constant ($F = 96485\ C\ mol^{-1}$), n_{O2} is the number of moles of O_2 produced estimated by ideal gas state equation. *Q* is the charge passed through the cell in the measurement time.

Computational details

Molecular dynamics (MD) simulations were carried out using the Forcite module in Materials Studio (MS). The COMPASS II force field[58] was utilized for interatomic potential calculations. Simulations were performed in the NPT ensemble at 300 K and 1 atm pressure, controlled using the Nosé–Hoover thermostat and barostat[59]. A simulation time of 6 ns with a timestep of 1 fs was adopted. Radial density distributions (RDS) were calculated based on trajectories obtained from the equilibrated system.

Density functional theory (DFT) calculations were performed using the Vienna Ab initio Simulation Package (VASP)[60]. The projector augmented wave (PAW) method[61] and the Perdew–Burke–Ernzerhof (PBE) functional[62] were employed. A plane-wave cutoff energy of 500 eV and a Monkhorst–Pack k-point grid[63] were used for all calculations. Structural optimizations and electronic structure analyses were conducted to obtain accurate electronic properties.

Data availability

The authors declare that all data supporting the results of this study are available within the paper and its Supplementary Information files or from the corresponding author upon request. Source data are provided with this paper.

References

1. Li, A. et al. Atomically dispersed hexavalent iridium oxide from MnO_2 reduction for oxygen evolution catalysis. *Science* **384**, 666–670 (2024).
2. Chong, L. et al. La- and Mn-doped cobalt spinel oxygen evolution catalyst for proton exchange membrane electrolysis. *Science* **380**, 609–616 (2023).
3. Buttler, A. & Spliethoff, H. Current status of water electrolysis for energy storage, grid balancing and sector coupling via power-to-gas and power-to-liquids: a review. *Renew. Sustain. Energy Rev.* **82**, 2440–2454 (2018).
4. Kong, S. et al. Acid-stable manganese oxides for proton exchange membrane water electrolysis. *Nat. Catal.* **7**, 252–261 (2024).
5. Yan, Q. et al. Chromium-induced high covalent Co–O bonds for efficient anodic catalysts in PEM electrolyzer. *Adv. Sci.* **11**, 2402356 (2024).
6. Wang, Y. et al. Tuning the Co pre-oxidation process of Co_3O_4 via geometrically reconstructed F–Co–O active sites for boosting acidic water oxidation. *Energy Environ. Sci.* **17**, 8820–8828 (2024).
7. Li, A. et al. Enhancing the stability of cobalt spinel oxide towards sustainable oxygen evolution in acid. *Nat. Catal.* **5**, 109–118 (2022).
8. Zhu, S. et al. Reconstructing hydrogen-bond network for efficient acidic oxygen evolution. *Angew. Chem. Int. Ed.* **63**, e202319462 (2024).
9. Lee, C. W. et al. Facet engineering of cobalt manganese oxide for highly stable acidic oxygen evolution reaction. *Adv. Energy Mater.* **15**, 2402786 (2024).
10. Shi, Z. et al. Enhanced acidic water oxidation by dynamic migration of oxygen species at the Ir/Nb_2O_{5-x} catalyst/support interfaces. *Angew. Chem. Int. Ed.* **61**, e202212341 (2022).
11. Gao, J., Tao, H. & Liu, B. Progress of nonprecious-metal-based electrocatalysts for oxygen evolution in acidic media. *Adv. Mater.* **33**, 2003786 (2021).
12. Lazaridis, T., Stühmeier, B. M., Gasteiger, H. A. & El-Sayed, H. A. Capabilities and limitations of rotating disk electrodes versus membrane electrode assemblies in the investigation of electrocatalysts. *Nat. Catal.* **5**, 363–373 (2022).
13. Mauritz, K. A. & Moore, R. B. State of understanding of nafion. *Chem. Rev.* **104**, 4535–4586 (2004).
14. Huang, X., Zhao, S., Liu, H., Wang, R. & Tang, H. Hydrophilic channel volume behavior on proton transport performance of proton exchange membrane in fuel cells. *ACS Appl. Polym. Mater.* **4**, 2423–2431 (2022).
15. Wan, R. et al. Earth-abundant electrocatalysts for acidic oxygen evolution. *Nat. Catal.* **7**, 1288–1304 (2024).
16. Lim, A. et al. Amphiphilic Ti porous transport layer for highly effective PEM unitized regenerative fuel cells. *Sci. Adv.* **7**, eabf7866 (2021).
17. Katzenberg, A. et al. Highly permeable perfluorinated sulfonic acid ionomers for improved electrochemical devices: insights into structure–property relationships. *J. Am. Chem. Soc.* **142**, 3742–3752 (2020).
18. Han, A. et al. Effect of cobalt ion contamination on proton conduction of ultrathin Nafion film. *Int. J. Hydrog. Energy* **45**, 25276–25285 (2020).
19. He, H. et al. Supramolecular modifying nafion with fluoroalkyl-functionalized polyoxometalate nanoclusters for high-selective proton conduction. *Angew. Chem. Int. Ed.* **63**, e202409006 (2024).
20. Manioglu, S. et al. Antibiotic polymyxin arranges lipopolysaccharide into crystalline structures to solidify the bacterial membrane. *Nat. Commun.* **13**, 6195 (2022).
21. Petrou, V. I. et al. Structures of aminoarabinose transferase ArnT suggest a molecular basis for lipid A glycosylation. *Science* **351**, 608–612 (2016).
22. Velkov, T., Thompson, P. E., Nation, R. L. & Li, J. Structure–activity relationships of polymyxin antibiotics. *J. Med. Chem.* **53**, 1898–1916 (2010).
23. Chen, F. et al. Blocking the sulfonate group in Nafion to unlock platinum's activity in membrane electrode assemblies. *Nat. Catal.* **6**, 392–401 (2023).

24. Asrafali, S. P., Periyasamy, T. & Kim, S.-C. Hydrophilic nature of polytetrafluoroethylene through modification with perfluorosulfonic acid-based polymers. *Sustainability* **15**, 16479 (2023).
25. Karimi, M. B., Mohammadi, F., Ghahramani, M. & Javanbakht, M. Fabrication and evaluation of electrospun nafion membranes as gel polymer electrolytes for high-performance lithium-ion batteries. *J. Phys. Chem. C.* **127**, 22943–22954 (2023).
26. Allen, F. I. et al. Morphology of hydrated as-cast nafion revealed through cryo electron tomography. *ACS Macro Lett.* **4**, 1–5 (2015).
27. Duan, Y. et al. Crosslinked PAEK-based nanofiber reinforced Nafion membrane with ion-paired interfaces towards high-concentration DMFC. *J. Membr. Sci.* **655**, 120589 (2022).
28. Ryu, S., Kim, J.-H., Lee, J.-Y. & Moon, S.-H. Investigation of the effects of electric fields on the nanostructure of Nafion and its proton conductivity. *J. Mater. Chem. A* **6**, 20836–20843 (2018).
29. Ke, C.-C. et al. Investigation on sulfuric acid sulfonation of in-situ sol–gel derived Nafion/SiO_2 composite membrane. *Int. J. Hydrog. Energy* **36**, 3606–3613 (2011).
30. Tsao, C. S., Chang, H. L., Jeng, U. S., Lin, J. M. & Lin, T. L. SAXS characterization of the Nafion membrane nanostructure modified by radiation cross-linkage. *Polymer* **46**, 8430–8437 (2005).
31. Mensharapov, R. M., Ivanova, N. A., Spasov, D. D., Grigoriev, S. A. & Fateev, V. N. SAXS investigation of the effect of freeze/thaw cycles on the nanostructure of Nafion® membranes. *Polymers* **14**, 4395 (2022).
32. Ryan, A. J., Stanford, J. L., Bras, W. & Nye, T. M. W. A synchrotron X-ray study of melting and recrystallization in isotactic polypropylene. *Polymer* **38**, 759–768 (1997).
33. Song, W. et al. Upscaled production of an ultramicroporous anion-exchange membrane enables long-term operation in electrochemical energy devices. *Nat. Commun.* **14**, 2732 (2023).
34. Zhang, Q. et al. Covalent organic framework–based porous ionomers for high-performance fuel cells. *Science* **378**, 181–186 (2022).
35. Liang, Y. et al. Stabilizing copper sites in coordination polymers toward efficient electrochemical C-C coupling. *Nat. Commun.* **14**, 474 (2023).
36. Hao, Y. et al. Recognition of surface oxygen intermediates on NiFe oxyhydroxide oxygen-evolving catalysts by homogeneous oxidation reactivity. *J. Am. Chem. Soc.* **143**, 1493–1502 (2021).
37. Pasquini, C. et al. H/D isotope effects reveal factors controlling catalytic activity in co-based oxides for water oxidation. *J. Am. Chem. Soc.* **141**, 2938–2948 (2019).
38. Huang, J. et al. Modifying redox properties and local bonding of Co_3O_4 by CeO_2 enhances oxygen evolution catalysis in acid. *Nat. Commun.* **12**, 3036 (2021).
39. Ahanjan, K., Shamsipur, M., Hassani, N., Neek-Amal, M. & Pashabadi, A. Oxygen vacancy-originated inorganic proton relay for the oxygen evolution reaction: fast proton hopping via La-doped praseodymium carbonate hydroxide. *J. Phys. Chem. C.* **127**, 24508–24522 (2023).
40. Hong, W. T. et al. Charge-transfer-energy-dependent oxygen evolution reaction mechanisms for perovskite oxides. *Energy Environ. Sci.* **10**, 2190–2200 (2017).
41. Koper, M. T. M. Theory of multiple proton–electron transfer reactions and its implications for electrocatalysis. *Chem. Sci.* **4**, 2710–2723 (2013).
42. Rebollar, L., Intikhab, S., Snyder, J. D. & Tang, M. H. Kinetic isotope effects quantify pH-sensitive water dynamics at the Pt electrode interface. *J. Phys. Chem. Lett.* **11**, 2308–2313 (2020).
43. Zhu, Z.-S. et al. Microenvironment engineering of heterogeneous catalysts for liquid-phase environmental catalysis. *Chem. Rev.* **124**, 11348–11434 (2024).
44. Fan, K. et al. Direct observation of structural evolution of metal chalcogenide in electrocatalytic water oxidation. *ACS Nano* **12**, 12369–12379 (2018).
45. Su, H. et al. Dynamic evolution of solid–liquid electrochemical interfaces over single-atom active sites. *J. Am. Chem. Soc.* **142**, 12306–12313 (2020).
46. Uzunova, E. L., Mikosch, H. & Nikolov, G. S. Electronic structure of oxide, peroxide, and superoxide clusters of the 3d elements: a comparative density functional study. *J. Chem. Phys.* **128**, 094307 (2008).
47. Lin, Y. et al. In situ identification and time-resolved observation of the interfacial state and reactive intermediates on a cobalt oxide nanocatalyst for the oxygen evolution reaction. *ACS Catal.* **12**, 5345–5355 (2022).
48. Cheng, W. et al. Lattice-strained metal–organic-framework arrays for bifunctional oxygen electrocatalysis. *Nat. Energy* **4**, 115–122 (2019).
49. Tang, L. et al. Operando identification of active sites in Co-Cr oxyhydroxide oxygen evolution electrocatalysts. *Nano Energy* **101**, 107562 (2022).
50. Hu, W. et al. Doping Ti into RuO_2 to accelerate bridged-oxygen-assisted deprotonation for acidic oxygen evolution reaction. *Adv. Mater.* **37**, 2411709 (2025).
51. Jin, H. et al. Dynamic rhenium dopant boosts ruthenium oxide for durable oxygen evolution. *Nat. Commun.* **14**, 354 (2023).
52. Lin, C. et al. In-situ reconstructed Ru atom array on α-MnO_2 with enhanced performance for acidic water oxidation. *Nat. Catal.* **4**, 1012–1023 (2021).
53. Wang, N. et al. Doping shortens the metal/metal distance and promotes OH coverage in non-noble acidic oxygen evolution reaction catalysts. *J. Am. Chem. Soc.* **145**, 7829–7836 (2023).
54. Kodama, K. et al. Effect of the side-chain structure of perfluorosulfonic acid ionomers on the oxygen reduction reaction on the surface of Pt. *ACS Catal.* **8**, 694–700 (2018).
55. Wang, X. et al. Sulfate-decorated amorphous–crystalline cobalt-iron oxide nanosheets to enhance O–O coupling in the oxygen evolution reaction. *ACS Nano* **17**, 825–836 (2023).
56. Niu, W. et al. Pb-rich Cu grain boundary sites for selective CO-to-n-propanol electroconversion. *Nat. Commun.* **14**, 4882 (2023).
57. Niu, W. et al. High-efficiency C_3 electrosynthesis on a lattice-strain-stabilized nitrogen-doped Cu surface. *Nat. Commun.* **15**, 7070 (2024).
58. Sun, H. COMPASS: an ab initio force-field optimized for condensed-phase applications overview with details on alkane and benzene compounds. *J. Phys. Chem. B* **102**, 7338–7364 (1998).
59. Nosé, S. A molecular dynamics method for simulations in the canonical ensemble. *Mol. Phys.* **52**, 255–268 (1984).
60. Kresse, G. & Furthmüller, J. Efficiency of ab-initio total energy calculations for metals and semiconductors using a plane-wave basis set. *Comput. Mater. Sci.* **6**, 15–50 (1996).
61. Blöchl, P. E. Projector augmented-wave method. *Phys. Rev. B* **50**, 17953–17979 (1994).
62. Perdew, J. P., Burke, K. & Ernzerhof, M. Generalized gradient approximation made simple. *Phys. Rev. Lett.* **77**, 3865–3868 (1996).
63. Monkhorst, H. J. & Pack, J. D. Special points for Brillouin-zone integrations. *Phys. Rev. B* **13**, 5188–5192 (1976).

Acknowledgements

This work was supported by NSFC (22279019 [B.Z.]), STCSM (25DZ3001100, 25DZ3001101, 25DZ3001102, 25DZ3001303 [B.Z.]), the National Key Research Program of China (Grant No. 2022YFA1503101 [Y.L.]) and Science and Technology Development Fund, Macau SAR (FDCT No. 0030/2022/AGJ [Y.L.]). The authors thank Guangrong Zhou and Prof. Yifei Xu for the assistance in the cryo-FIB-SEM characterizations. The authors thank Hui Tang for the assistance in the SAXS and DSC measurements. The authors thank Wenjuan Shi, Chenyang Wei, Siqi Yang and Prof. Xueyan Feng for providing suggestions for experiments. The authors also appreciate the Shiyanjia Lab (www.shiyanjia.com) for the XPS and HAADF-STEM tests.

Author contributions

B.Z. supervised this work. Q.Y. and C.L. contributed equally to this work. Q.Y. conceived and designed the experiments. Q.Y. synthesized the materials, measured the electrochemical performance, conducted the characterizations, carried out corresponding in situ spectroscopies and write the paper. C.L. and. Y.L. performed the DFT calculations and MD simulations. W.L., K.S. and W.N. provided suggestions for article revision. Y.Z., N.H. and J.-Y.C. assisted in PEMWE, proton conductivity and ^{1}H NMR measurements. K.S. participated in the in situ ATR-SEIRAS measurements. X.Y. and J.-F.C. assisted in FE measurements. Y.H. participated in SEM tests. Z.L. assisted in XRD measurements. All of the authors discussed the results and commented on the manuscript.

Competing interests

The authors declare no competing interests.

Additional information

Supplementary information The online version contains supplementary material available at https://doi.org/10.1038/s41467-025-64599-1.

Correspondence and requests for materials should be addressed to Bo Zhang.

Peer review information *Nature Communications* thanks Shichun Mu, Jian Xie and the other, anonymous, reviewer(s) for their contribution to the peer review of this work. A peer review file is available.

Reprints and permissions information is available at http://www.nature.com/reprints

Publisher's note Springer Nature remains neutral with regard to jurisdictional claims in published maps and institutional affiliations.